PHYSICAL REVIEW LETTERS

Probing Three-Body Correlations in a Quantum Gas Using the Measurement of the Third Moment of Density Fluctuations

J. Armijo,[1] T. Jacqmin,[1] K. V. Kheruntsyan,[2] and I. Bouchoule[1]

[1]*Laboratoire Charles Fabry, UMR 8501 du CNRS, Institut d'Optique, 91 127 Palaiseau Cedex, France*
[2]*ARC Centre of Excellence for Quantum-Atom Optics, School of Mathematics and Physics, University of Queensland,
Brisbane, Queensland 4072, Australia*
(Received 20 July 2010; published 30 November 2010)

We perform measurements of the third moment of atom number fluctuations in small slices of a very elongated weakly interacting degenerate Bose gas. We find a positive skewness of the atom number distribution in the ideal gas regime and a reduced skewness compatible with zero in the quasicondensate regime. For our parameters, the third moment is a thermodynamic quantity whose measurement constitutes a sensitive test of the equation of state, and our results are in agreement with a modified Yang-Yang thermodynamic prediction. Moreover, we show that the measured skewness reveals the presence of true three-body correlations in the system.

Measurements of higher-order correlations and the density fluctuations, in particular, are becoming an increasingly important tool in the studies of ultracold quantum gases. Such measurements are able to probe quantum many-body states of interacting systems, often giving access to key quantities that characterize the system. This is particularly true for one-dimensional (1D) gases, where the effects of fluctuations are enhanced compared to 3D systems and govern the rich underlying physics. Zero-distance second- and third-order correlation functions have been probed in several ultracold gas experiments by measuring the rates of two- and three-body inelastic processes such as photoassociation and three-body recombination [1–3]. Such measurements enabled the study of the strongly correlated regime of "fermionization" in a 1D Bose gas.

An alternative experimental technique is the *in situ* measurement of atom number fluctuations in a small detection volume, achievable through the analysis of noise in absorption images. The fluctuation variance (or second moment) provides information about an integrated nonlocal density-density correlation function. In addition, under adequate experimental conditions, the variance can render as a thermodynamic quantity, and therefore such measurements constitute a probe of the thermodynamic properties of quantum gases [4–6], alternative to the analysis of density profiles [7–9] or momentum distributions [10]. *In situ* measurements of atom number fluctuations in weakly interacting quasi-1D Bose gases were used to probe the crossover from the nearly ideal gas regime, where bosonic bunching is present, to the quasicondensate regime, where the density fluctuations are suppressed [4,6]. In fermionic systems, sub-shot-noise atom number fluctuations were observed in a degenerate Fermi gas [11,12]. Combining this with the measurement of compressibility of the gas deduced from the known density profile and confining potential,

such measurements have been shown to provide reliable thermometry [11].

In this Letter we expand the arsenal of probes of higher-order correlations in quantum gases by measuring the third moment of atom number fluctuations. This is done using *in situ* absorption imaging of an ultracold gas on an atom-chip setup sketched in Fig. 1(a). We probe a weakly interacting quasi-1D Bose gas. We have measured a positive third moment of the atom number distribution in a degenerate gas within the ideal gas regime and within the crossover towards a quasicondensate. In the quasicondensate regime the measured third moment is compatible with zero. The third moment of the atom number distribution is linked to the third-order correlation function, and our measurements demonstrate the presence of true three-body correlations in the gas. Apart from this, we show that the measured third moment is related to a thermodynamic relation that involves a second-order
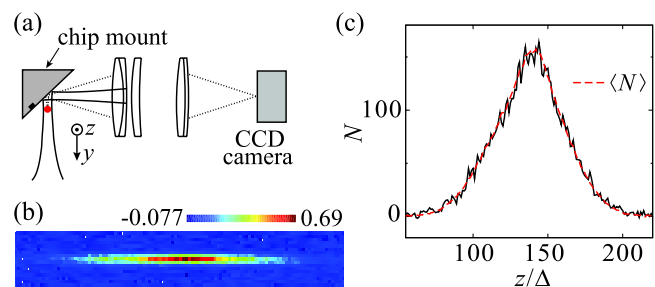

FIG. 1 (color online). (a) Scheme of the imaging setup. The probe laser crosses the atomic cloud (red dot) before its reflection from the chip surface and detection on a CCD camera. (b) Typical *in situ* absorption image; the scale on the color bar shows the optical density. The pixel size in the object plane is $\Delta = 4.5\ \mu$m. (c) Typical longitudinal density profile (solid curve), together with the mean profile (dashed red curve).

derivative, and therefore the technique can be used as a sensitive probe of the thermodynamics of a quantum gas.

Our quasi-1D Bose gases are produced using ^{87}Rb atoms in the hyperfine state $|F = 2, m = 2\rangle$. A very elongated Ioffe magnetic trap with a longitudinal oscillation frequency ranging from 5.0 to 8 Hz and a transverse oscillation frequency $\omega_\perp/2\pi$ ranging from 3 to 4 kHz is realized using on-chip microwires and an external homogeneous magnetic field. Using rf evaporation, we produce ultracold clouds at temperatures from $T = 20$ to 500 nK. The longitudinal rms size L of the cloud ranges from ~50 to ~100 μm. Under these conditions such gases explore the crossover from the ideal gas regime to the quasicondensate regime [4], and the underlying physics lies in the 1D regime or in the crossover from 1D to 3D [6].

In situ measurements of density fluctuations are performed using absorption images such as the one shown in Fig. 1(b). The details of our imaging and calibration techniques are described in the supplementary material [13]. As the transverse size of the trapped cloud (< 500 nm rms) is much smaller than the pixel size (4.5 μm), the only information in the transverse direction is the diffractional and motional blur on the image. By summing the atom number over transverse pixels, we reduce the notion of a pixel to a segment of length Δ and derive from each image the longitudinal density profile [Fig. 1(c)]. We perform a statistical analysis of hundreds of images taken under the same experimental conditions [4,6]. For each profile and pixel we extract $\delta N = N - \langle N \rangle$, where $\langle N \rangle$ is given by the average density profile. To remove the effect of shot-to-shot variations in the total atom number N_{tot}, the profiles are ordered according to N_{tot} and we use a running average of about 20 profiles. As will be explained below, the longitudinal confining potential is irrelevant and each δN is binned according to the corresponding mean atom number in the pixel $\langle N \rangle$. For each bin, we compute the second and third moment of atom number fluctuations, $\langle \delta N^2 \rangle$ and $\langle \delta N^3 \rangle$. The contribution of the optical shot noise to these quantities is subtracted, although it is negligible for $\langle \delta N^3 \rangle$.

The measured third moment of the atom number fluctuations, $\langle \delta N^3 \rangle_m$, is plotted in Fig. 2 for two different temperatures. For the higher temperature [Fig. 2(a)], we observe a positive value of $\langle \delta N^3 \rangle_m$ that increases with $\langle N \rangle$. At a smaller temperature [Fig. 2(b)], $\langle \delta N^3 \rangle_m$ initially grows with $\langle N \rangle$ and reaches a maximum, before taking a value compatible with zero at large $\langle N \rangle$. The corresponding second moments or variances $\langle \delta N^2 \rangle_m$ are shown in the insets. A finite third moment indicates an asymmetry of the atom number distribution, which is usually quantified by the skewness $s_m = \langle \delta N^3 \rangle_m / \langle \delta N^2 \rangle_m^{3/2}$, shown in Figs. 2(c) and 2(d). Before discussing the physics behind these results, we first describe how the *measured* moments $\langle \delta N^3 \rangle_m$ and $\langle \delta N^2 \rangle_m$ are related to the *true* moments $\langle \delta N^3 \rangle$ and $\langle \delta N^2 \rangle$.

The measurements of atom number fluctuations are affected by the finite spatial resolution due to both the
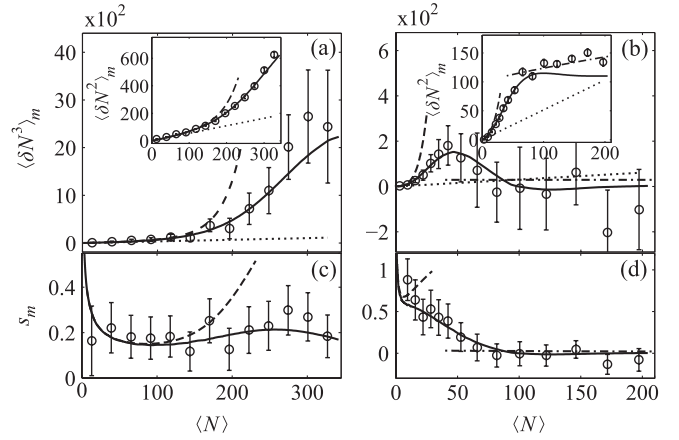

FIG. 2. Measured third moment (open circles) of the atom number fluctuations versus the mean atom number per pixel, for temperatures of 376 nK (a) and 96 nK (b). The insets show the corresponding atom number variances. The error bars are the statistical errors. Graphs (c) and (d) show the skewness s_m corresponding to (a) and (b), respectively. The theoretical predictions, scaled by $\kappa_2 = 0.55$ and $\kappa_3 = 0.34$ for (a) and (c), and by $\kappa_2 = 0.52$ and $\kappa_3 = 0.31$ for (b) and (d), are shown for comparison: solid lines, the modified Yang-Yang prediction; dashed lines, the ideal Bose-gas prediction; dash-dotted lines on (b) and (d), the quasicondensate prediction; dotted lines, the shot-noise limit $\langle N \rangle$.

optical resolution and the diffusion of atoms during the optical pulse, which cause the absorption signal from each atom to spread over several pixels and blur the image. Denoting by $\mathcal{A}$ the impulse response function of the imaging system, the impulse response for the pixel $[0, \Delta]$ is $\mathcal{F}(z_0) = \int_0^\Delta dz \mathcal{A}(z - z_0)$, and the measured atom number fluctuation in the pixel is given by $\delta N_m = \int_{-\infty}^{+\infty} dz_0 \mathcal{F}(z_0) \delta n(z_0)$, where $\delta n(z_0)$ is the local density fluctuation. For the parameters explored in this Letter, the expected correlation length l_c of density fluctuations [14] is smaller than 0.5 μm. This is sufficiently smaller than the width of $\mathcal{A}$ so that we can assume that the density fluctuations have zero range. Moreover, since the resolution and the pixel size are much smaller than the longitudinal size of the cloud, we can assume that the gas is locally homogeneous with respect to z. Then, the measured second and third moments can be obtained as

$$\langle \delta N^2 \rangle_m = \langle \delta N^2 \rangle \int_{-\infty}^{+\infty} dz_0 \mathcal{F}(z_0)^2/\Delta = \kappa_2 \langle \delta N^2 \rangle, \quad (1)$$

$$\langle \delta N^3 \rangle_m = \langle \delta N^3 \rangle \int_{-\infty}^{+\infty} dz_0 \mathcal{F}(z_0)^3/\Delta = \kappa_3 \langle \delta N^3 \rangle, \quad (2)$$

where $\langle \delta N^2 \rangle$ and $\langle \delta N^3 \rangle$ are the respective true moments, whereas κ_2 and κ_3 are the reduction factors. For low enough linear densities, the gas lies in the nondegenerate ideal gas regime. Then the fluctuations are almost that of a Poissonian distribution, so that $\langle \delta N^2 \rangle \simeq \langle \delta N^3 \rangle \simeq \langle N \rangle$, and the reduction factors may be deduced from a linear fit of the measured fluctuations versus $\langle N \rangle$, where $\langle N \rangle$ is experimentally determined absolutely. However, such a

deduction is difficult in very cold clouds where only a few pixels lie in the nondegenerate ideal gas regime.

We thus develop an alternative method that uses the measurement of the atom number correlation

$$C_{i,i+j} = \frac{\langle \delta N_i \delta N_{i+j} \rangle_m}{\langle \delta N_i^2 \rangle_m} = \frac{\int_{-\infty}^{+\infty} dz_0 \mathcal{F}(z_0) \mathcal{F}(z_0 - j\Delta)}{\int_{-\infty}^{+\infty} dz_0 \mathcal{F}(z_0)^2} \quad (3)$$

between the pixel i and the adjacent ($j = 1$) or the next-neighbor ($j = 2$) pixels. Such correlation arises due to the contribution of an atom to the absorption in both pixels. Making a Gaussian ansatz for the impulse response function $\mathcal{A}$, the rms width of $\mathcal{A}$ can obtained by fitting Eq. (3) to the measured correlations $C_{i,i+1}$ [13]. The reduction factors $\kappa_{2,3}$ can then be deduced from Eqs. (1) and (2), resulting typically in $\kappa_3 \simeq 0.3$ and $\kappa_2 \simeq 0.5$ for our data. The result is in good agreement with the slope of $\langle \delta N^2 \rangle_m$ at small $\langle N \rangle$ [see the inset of Fig. 2(a)].

Turning to the discussion of the physics behind our experimental results, we first point out that the third moment of atom number fluctuations is actually a thermodynamic quantity when, as in our experiment, the pixel size is both much larger than the characteristic correlation length of density fluctuations l_c and much smaller than the cloud length L, $l_c \ll \Delta \ll L$. Then a local density approximation is valid and the gas contained in a pixel can be well described by a grand-canonical ensemble, in which the rest of the cloud is acting as a reservoir that fixes the chemical potential μ and the temperature T. Denoting by Z the grand-canonical partition function, we have $\langle N \rangle = (k_B T/Z) \partial Z/\partial \mu$, $\langle N^2 \rangle = (k_B^2 T^2/Z) \partial^2 Z/\partial \mu^2$, and $\langle N^3 \rangle = (k_B^3 T^3/Z) \partial^3 Z/\partial \mu^3$. From the first two equations, we obtain the well-known thermodynamics relation $\langle \delta N^2 \rangle = k_B T \partial \langle N \rangle / \partial \mu$, whereas the three equations give

$$\langle \delta N^3 \rangle = (k_B T)^2 \partial^2 \langle N \rangle / \partial \mu^2, \quad (4)$$

where $\langle N \rangle = n\Delta$ and n is the linear density of a gas homogeneous along z. Thus, the knowledge of the equation of state (EOS) $n = n(\mu, T)$ is sufficient to predict the third moment of the atom number distribution. Note that a more traditional form of the EOS for pressure P can be readily deduced from $n(\mu, T)$ using the Gibbs-Duhem relation, $n = (\partial P/\partial \mu)_T$, leading to $P = \int_{-\infty}^{\mu} n(\mu', T) d\mu'$.

We now compare our measurements with the predictions from different models for the EOS $n(\mu, T)$. The temperature of the cloud for the case of Fig. 2(a) is deduced from an ideal Bose gas fit to the wings of the density profile [6]. For the data of Fig. 2(b), corresponding to the quasicondensate regime, such wings are vanishingly small and hard to detect. In this case we deduce the temperature [6] from the measurement of density fluctuations in the cloud center using the thermodynamic relation $\langle \delta N^2 \rangle = k_B^2 T^2 \partial \langle N \rangle / \partial \mu$ and the EOS of a quasicondensate (see below).

The predictions from the equation of state for an ideal Bose gas are shown by the dashed lines in Fig. 2. For a highly nondegenerate (or classical) gas, corresponding to small $\langle N \rangle$, this model predicts $\langle \delta N^3 \rangle \simeq \langle \delta N^2 \rangle \simeq \langle N \rangle$ as

expected for a gas of uncorrelated particles. When the gas becomes degenerate with the increase of $\langle N \rangle$, the contribution of the quantum-statistical exchange interaction term to $\langle \delta N^3 \rangle$ is no longer negligible, and $\langle \delta N^3 \rangle$ becomes larger than the shot-noise term $\langle N \rangle$. Such an increase is observed in the experimental data in Fig. 2(a). However, the ideal Bose-gas model strongly overestimates the third moment with further increase of $\langle N \rangle$ and we eventually observe large discrepancy between the predictions of this model and the experimental data. The discrepancy is due to the repulsive interactions between the atoms, which reduce the energetically costly density fluctuations.

Describing the effects of atomic interactions beyond the perturbative regime is a challenging theoretical problem. However, a 1D Bose gas with contact repulsive interactions is particular since the model is exactly solvable, in the entire parameter space, using the Yang-Yang thermodynamic formalism [15]. For the temperatures corresponding to Figs. 2(a) and 2(b), the ratios of $k_B T/\hbar\omega_\perp$ are 2.6 and 0.50, respectively, implying that the population of the transverse excited states is not negligible. Accordingly, we use a *modified* Yang-Yang model [7], in which the transverse ground state is described within the exact Yang-Yang theory [16], whereas the transverse excited states are treated as ideal 1D Bose gases. This model has been shown to be valid for our parameters until the quasicondensate regime is reached [6]. The corresponding predictions are plotted in Fig. 2 and agree with the measured $\langle \delta N^3 \rangle$ very well.

In the quasicondensate regime [corresponding to $\langle N \rangle \gtrsim 70$ in Fig. 2(b)], where the density fluctuations are suppressed [17,18], the EOS can be obtained numerically from the 3D Gross-Pitaevskii equation and is well described by the heuristic function $\mu = \hbar\omega_\perp(\sqrt{1 + 4na} - 1)$ [19]. In contrast to the modified Yang-Yang model, this EOS accounts for the transverse swelling of the cloud due to interatomic interactions and better describes the measured variance [see the inset of Fig. 2(b)]. The measured third moment is compatible with this EOS.

To unveil the role of many-body correlations, which underlie the measured density fluctuations while remaining hidden in the thermodynamic analysis, we consider the 1D two- and three-body ($k = 2, 3$) correlation functions,

$$\tilde{g}^{(k)}(z_1, \ldots, z_k) = \langle \tilde{\psi}^\dagger(z_1) \cdots \tilde{\psi}^\dagger(z_k) \tilde{\psi}(z_k) \cdots \tilde{\psi}(z_1) \rangle / n^k,$$

where $\tilde{\psi}(z) = \int dx dy \, \psi(x, y, z)$ and ψ is the bosonic field operator. Using standard commutation relations and the expression $\langle N^2 \rangle = \langle N \rangle^2 + \langle N \rangle + n^2 \iint dz_1 dz_2 [\tilde{g}^{(2)}(z_1, z_2) - 1]$, we find

$$\langle \delta N^3 \rangle = \langle N \rangle + n^3 \iiint dz_1 dz_2 dz_3 [\tilde{g}^{(3)}(z_1, z_2, z_3) - 1]$$

$$- 3\langle N \rangle n^2 \iint dz_1 dz_2 [\tilde{g}^{(2)}(z_1, z_2) - 1]$$

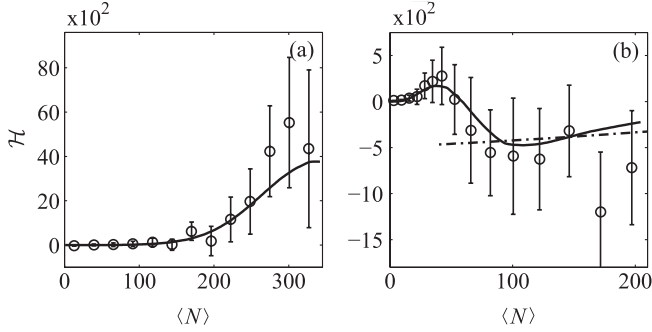$$+ 3n^2 \iint dz_1 dz_2 [\tilde{g}^{(2)}(z_1, z_2) - 1], \quad (5)$$

FIG. 3.   The measured three-body integral $\mathcal{H}_m$ versus $\langle N \rangle$, corresponding to the data of Figs. 2(a) and 2(b), respectively. The solid (dash-dotted) curves are the thermodynamic predictions from the modified Yang-Yang (quasicondensate) model.

where the integrals are in the interval $[0, \Delta]$. As we see, the third moment of atom number distribution depends on both the $\tilde{g}^{(3)}$ and $\tilde{g}^{(2)}$ functions. Moreover, $\tilde{g}^{(3)}$ contains a contribution from $\tilde{g}^{(2)}$ since, when one of the three particles is far from the other two, $\tilde{g}^{(3)}$ reduces to $\tilde{g}^{(2)}$. To remove such contributions, we introduce the h function

$$h(z_1, z_2, z_3) = 2 + \tilde{g}^{(3)}(z_1, z_2, z_3) - [\tilde{g}^{(2)}(z_1, z_2)$$
$$+ \tilde{g}^{(2)}(z_2, z_3) + \tilde{g}^{(2)}(z_1, z_3)], \qquad (6)$$

which is nonzero only for all z_i being in the vicinity of each other. Such a decomposition has been previously used in the description of weakly correlated plasmas [20], with the approximation $h \simeq 0$ being used to truncate the Bogoliubov-Born-Green-Kirkwood-Yvon hierarchy.

Using the h function, Eq. (5) can be rewritten as

$$\langle \delta N^3 \rangle = \langle N \rangle + 3n^2 \iint dz_1 dz_2 [\tilde{g}^{(2)}(z_1, z_2) - 1]$$
$$+ n^3 \iiint dz_1 dz_2 dz_3 h(z_1, z_2, z_3). \qquad (7)$$

Here, the first two terms represent one- and two-body effects, with the second term being equal to $3\langle \delta N^2 \rangle - 3\langle N \rangle$. The contribution of *true* three-body correlations to $\langle \delta N^3 \rangle$ comes from the three-body integral

$$\mathcal{H} = \langle \delta N^3 \rangle + 2\langle N \rangle - 3\langle \delta N^2 \rangle$$
$$= n^3 \iiint dz_1 dz_2 dz_3 h(z_1, z_2, z_3). \qquad (8)$$

In Fig. 3, we plot the measured value of $\mathcal{H}$. More precisely, taking into account the reduction factors κ_2 and κ_3, we plot $\mathcal{H} = \langle \delta N^3 \rangle_m / \kappa_3 + 2\langle N \rangle - 3\langle \delta N^2 \rangle_m / \kappa_2$. We observe nonzero values of $\mathcal{H}$, which is a signature of the presence of true three-body correlations in the gas: $\mathcal{H}$ is positive within the ideal gas regime and in the crossover region towards the quasicondensate [see Fig. 3(a)], whereas it is negative in the quasicondensate regime [Fig. 3(b)]. The results are in agreement with the

thermodynamic predictions of the modified Yang-Yang and the quasicondensate models.

In summary, we have measured the third moment of density fluctuations in an ultracold quantum gas. This quantity reveals the presence of true three-body correlations in the system. Moreover, for sufficiently large pixels, such measurements constitute a very sensitive probe of the thermodynamics of the gas. As the third moment is related to the second-order derivative of $n(\mu, T)$, the method lends itself as a high-precision tool for discriminating between alternative theoretical models and can be applied to a broad class of ultracold atom systems. For example, intriguing opportunities are in the understanding of the role of higher-order correlations in thermalization of isolated quantum systems [21] and in the study of thermodynamics of more exotic many-body systems where three-body effects, such as Efimov resonances [22], may lead to different signatures in the second- and third-order correlations.

[1] E. A. Burt *et al.*, Phys. Rev. Lett. **79**, 337 (1997).
[2] B. Laburthe Tolra *et al.*, Phys. Rev. Lett. **92**, 190401 (2004).
[3] T. Kinoshita, T. Wenger, and D. S. Weiss, Phys. Rev. Lett. **95**, 190406 (2005).
[4] J. Estève *et al.*, Phys. Rev. Lett. **96**, 130403 (2006).
[5] C.-L. Hung *et al.*, arXiv:1009.0016.
[6] J. Armijo *et al.*, arXiv:1011.3631.
[7] A. H. van Amerongen *et al.*, Phys. Rev. Lett. **100**, 090402 (2008).
[8] S. P. Rath *et al.*, Phys. Rev. A **82**, 013609 (2010).
[9] S. Nascimbène *et al.*, Nature (London) **463**, 1057 (2010); N. Navon *et al.*, Science **328**, 729 (2010).
[10] J. T. Stewart *et al.*, Phys. Rev. Lett. **104**, 235301 (2010).
[11] T. Müller *et al.*, Phys. Rev. Lett. **105**, 040401 (2010).
[12] C. Sanner *et al.*, Phys. Rev. Lett. **105**, 040402 (2010).
[13] See supplementary material at http://link.aps.org/supplemental/10.1103/PhysRevLett.105.230402 for imaging and calibration techniques.
[14] P. Deuar *et al.*, Phys. Rev. A **79**, 043619 (2009).
[15] C. N. Yang and C. P. Yang, J. Math. Phys. (N.Y.) **10**, 1115 (1969).
[16] I. Bouchoule, K. V. Kheruntsyan, and G. V. Shlyapnikov, Phys. Rev. A **75**, 031606(R) (2007).
[17] C. Mora and Y. Castin, Phys. Rev. A **67**, 053615 (2003).
[18] K. V. Kheruntsyan *et al.*, Phys. Rev. Lett. **91**, 040403 (2003).
[19] J. N. Fuchs, X. Leyronas, and R. Combescot, Phys. Rev. A **68**, 043610 (2003).
[20] T. J. M. Boyd and J. J. Sanderson, *The Physics of Plasmas* (Cambridge University Press, Cambridge, 2003).
[21] A. Giraud and J. Serreau, Phys. Rev. Lett. **104**, 230405 (2010); D. Muth *et al.*, New J. Phys. **12**, 083065 (2010).
[22] T. Krämer *et al.*, Nature (London) **440**, 315 (2006).

Probing three-body correlations in a quantum gas using the measurement of the third moment of density fluctuations:
Precise measurement of the atomic density profile and determination of imaging resolution

J. Armijo[(1)], T. Jacqmin[(1)], K. V. Kheruntsyan[(2)], and I. Bouchoule[(1)]

[(1)]*Laboratoire Charles Fabry, UMR 8501 du CNRS,*
Institut d'Optique, 91 127 Palaiseau Cedex, France
[(2)]*ARC Centre of Excellence for Quantum-Atom Optics, School of Mathematics and Physics,*
University of Queensland, Brisbane, Queensland 4072, Australia

A probe laser beam, locked onto the D_2 transition at the wavelength $\lambda = 780$ nm, is reflected from the chip surface (covered by a gold mirror) after passing through the atomic cloud. The shadow image of the atomic cloud is then recorded on a CCD camera, with quantum efficiency larger than 90%. The diffraction-limited optical resolution has an rms width of 1.0 μm. Great care has to be taken in absorption imaging to allow for a reliable measurement of the atom number in each pixel.

We have chosen a configuration that maximizes the absorption efficiency. To achieve this, we focus the probe beam onto the chip surface using a cylindrical lens as depicted in Fig. 1 (a) of the main text. The $1/e^2$ size of the beam in the focused direction x is 50 μm, which is smaller than the distance of the atomic cloud from the chip surface so that the beam crosses the atomic cloud only on its way to the chip and not after its reflection. Images as in Fig. 1 (a)-(c) are taken after switching off the wire currents so that only the external homogeneous magnetic field, whose orientation is close to the y direction [see Fig. 1 (a) of the main text for the axis definition], remains switched on. With this geometry, using a σ_+-polarized probe beam we address only the closed transition $|F = 2, m = 2\rangle \rightarrow |F' = 3, m' = 3\rangle$, and the absorption cross-section at low intensity takes its maximum value $\sigma_0 = 3\lambda^2/2\pi$.

The absorption is measured by taking two pictures, the first one with the atomic cloud present and the second one without the atoms. The atom number in a given pixel N_p is estimated from the Beer-Lambert law $N_p = \ln(N_2/N_1)\Delta^2/\sigma$, where N_1 and N_2 are the photon numbers in the pixel on the first and second image, respectively, and σ is the atomic absorption cross-section. With the transverse size of the cloud being smaller than the pixel size, no information is available in the transverse direction, and the number of atoms N_{BL} in an effective pixel of size Δ can be obtained by summing N_p over of the transverse pixels. However, as the use of a resonant probe at high atomic densities produces high optical densities (up to 1.5) this naive procedure fails to correctly estimate the true atom number N in the pixel. Firstly, when the transverse extension of the cloud is smaller than
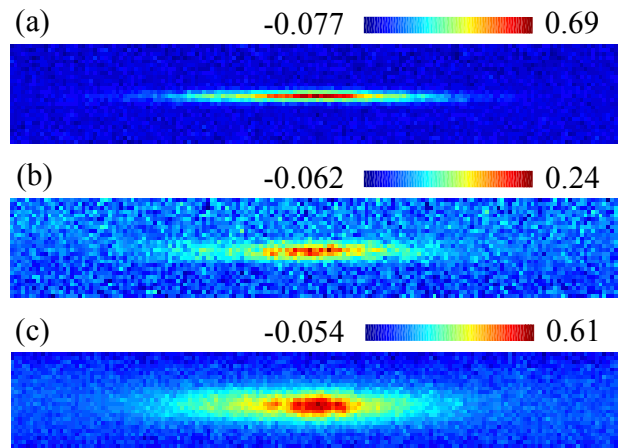

FIG. 1: (Color online) Typical absorption images used for calibration and the analysis of density fluctuations: (a) – taken with a nearly resonant probe, after a small time of flight of 0.5 ms [same as Fig. 1 (b) of the main text, except with a larger field of view]; (b) – taken with a probe detuned by 5 MHz and a time of flight of 1.5 ms; (d) – taken with a resonant probe and a time of flight of 2.2 ms to measure the total atom number. The scales on the colorbars correspond to optical densities.

both the pixel size and the optical resolution, the Beer-Lambert law underestimates the true atom number due to the concavity of the logarithm function, as already pointed out in [1]. Moreover, the validity of the Beer-Lambert law is questionable for high atomic densities due to nontrivial reabsorption effects that may arise [2]. In order to reduce these effects, without decreasing too much the absorption, we use a near resonant probe and enable the cloud to spread transversally during a small time of flight of about 0.5 ms – sufficient to reduce the effects of high atomic densities, but small enough so that the atom number fluctuations in a pixel are barely affected. The measured atom number N_{BL}, however, still deviates from the true atom number N and we introduce a function f defined as $N = f(N_{BL})$ to describe the deviation from linearity at high optical densities.

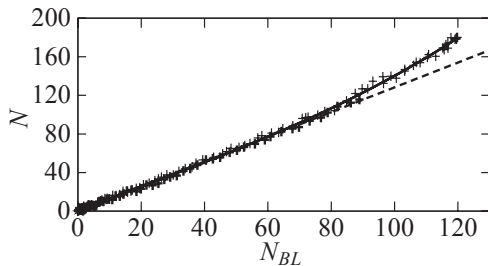The function f is deduced from the comparison, in

FIG. 2: Experimental determination of the correction to the Beer-Lambert law. The solid curve is a fit to the experimental data with a third-order polynomial, the straight dashed line being the linear contribution. N_{BL} is obtained by using the Beer-Lambert law and summing over transverse pixels in images taken with a nearly resonant probe and a small time of flight of 0.5 ms [see Fig. 1 (a)]. N is obtained from images taken with a probe detuned by 5 MHz and a time of flight of 1.5 ms, for which the Beer-Lambert law is adequate [see Fig. 1 (b)].

each effective pixel, of the measured N_{BL} with the correct atom number N. The latter itself is measured as follows. First, the correct profile is obtained using images [such as that shown in Fig. 1 (b)] taken with a detuning of about 5 MHz that reduces the absorption cross-section and a time of flight of ~ 1.5 ms that permits a transverse expansion of the cloud. We checked experimentally that these parameters ensure the validity of the Beer-Lambert law, while the expansion is small enough as to retain the longitudinal profile essentially unaffected. Second, the absolute normalization of the atomic density profile (or, equivalently, a measure of the absorption cross-section σ), is deduced form the knowledge of the total atom number. The latter is measured using a resonant probe with a time of flight of ~ 2.5 ms, as in Fig. 1 (c). With such time of flight, the cloud transverse expansion is sufficiently large and the atomic density is small enough as to render the Beer-Lambert law applicable. Atomic saturation is taken into account via the formula $\sigma = \sigma_0(1 + I/I_{\text{sat}})$, where I is the intensity of the probe beam and I_{sat} is the saturation intensity. A fit of the measured absorption versus I gives $I_{\text{sat}} = 1.4(1)$ mW/cm^2, which is close to the reported value of 1.62 mW/cm^2 [3]. The remaining discrepancy could be because of possible underestimation of the intensity of the probe beam seen by the atoms due to the losses during the reflection of the beam from the gold mirror and during the transmission through the optical lenses. Finally, the function f is estimated by fitting the experimental points N versus N_{BL} with a third-order polynomial, as shown in Fig. 2.

All these calibrations are performed using values averaged over tens of experimental realizations. The images used for the analysis of fluctuations [as in Fig. 1 (a)] and those used for calibration [as in Figs. 1 (b) and (c)] are

taken in an alternated way – typically one picture of type (b) and then (c) after every 15 images of type (a) – to eliminate the dependence on noise arising from long-time magnetic field and thermal drifts.

The normalization procedure described above, while compensating for the effect of the small transverse size of the atomic cloud, does not compensate for a possible error induced by short-scale longitudinal density fluctuations. However, in our experimental situation, those fluctuations are smeared out by the atomic diffusion during the probe pulse and are small.
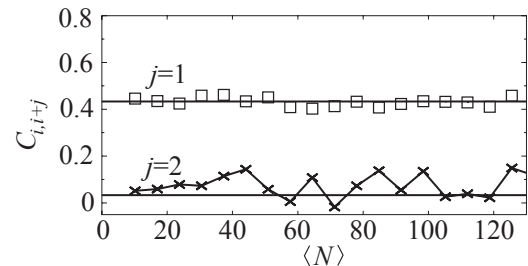

FIG. 3: Correlation of atom number fluctuations between adjacent (open squares) and next-neighbor (crosses) pixels. The solid lines are the predictions for an impulse response function with an rms width of 2.0 μm, obtained by fitting $C_{i,i+1}$.

The precise calibration of the atom number measurement described above is not sufficient for the analysis of atom number fluctuations. Indeed, the fluctuations are affected by a finite spatial resolution due to both the optical resolution and the diffusion of atoms during the optical pulse, which cause the absorption signal from each atom to spread over several pixels and blur the image (see main text). The finite spatial resolution is also responsible for a nonvanishing correlation between the atom numbers measured in nearby pixels. In fact, we make use of this correlation for experimental determination of the spatial resolution of our imaging system. In Fig. 3 we show the experimental data for the correlation coefficients $C_{i,i+j}$ [see Eq. (3) of the main text], corresponding to the atom number fluctuations in the adjacent ($j = 1$) and next-neighboring ($j = 2$) pixels, for the experimental data of Fig. 2 (c) of the main text. Fitting these correlation coefficients, we extract the rms width δ of the impulse response function $\mathcal{A}$ and we find that $\delta = 2.0$ μm for this data set.

[1] J. Esteve *et al.*, Phys. Rev. Lett. **96**, 130403 (2006).
[2] S. P. Rath *et al.*, Phys. Rev. A **82**, 013609 (2010).
[3] http://steck.us/alkalidata/